

Enhancing coherence in molecular spin qubits via atomic clock transitions

Muhandis Shiddiq^{1*}, Dorsa Komijani^{1*}, Yan Duan², Alejandro Gaita-Ariño², Eugenio Coronado² & Stephen Hill¹

Quantum computing is an emerging area within the information sciences revolving around the concept of quantum bits (qubits). A major obstacle is the extreme fragility of these qubits due to interactions with their environment that destroy their quantumness. This phenomenon, known as decoherence, is of fundamental interest^{1,2}. There are many competing candidates for qubits, including superconducting circuits³, quantum optical cavities⁴, ultracold atoms⁵ and spin qubits^{6–8}, and each has its strengths and weaknesses. When dealing with spin qubits, the strongest source of decoherence is the magnetic dipolar interaction⁹. To minimize it, spins are typically diluted in a diamagnetic matrix. For example, this dilution can be taken to the extreme of a single phosphorus atom in silicon⁶, whereas in molecular matrices a typical ratio is one magnetic molecule per 10,000 matrix molecules¹⁰. However, there is a fundamental contradiction between reducing decoherence by dilution and allowing quantum operations via the interaction between spin qubits. To resolve this contradiction, the design and engineering of quantum hardware can benefit from a ‘bottom-up’ approach whereby the electronic structure of magnetic molecules is chemically tailored to give the desired physical behaviour. Here we present a way of enhancing coherence in solid-state molecular spin qubits without resorting to extreme dilution. It is based on the design of molecular structures with crystal field ground states possessing large tunnelling gaps that give rise to optimal operating points, or atomic clock transitions, at which the quantum spin dynamics become protected against dipolar decoherence. This approach is illustrated with a holmium molecular nanomagnet in which long coherence times (up to 8.4 microseconds at 5 kelvin) are obtained at unusually high concentrations. This finding opens new avenues for quantum computing based on molecular spin qubits.

One of the proposed approaches to obtaining spin qubits is that of using magnetic molecules^{8–16}. Up to now, coherence has been optimized through dilution and deuteration to minimize dipolar and hyperfine interactions, respectively^{9–11,13,16}. A class of molecules in which these two sources of decoherence can be minimized by alternative means are the so-called polyoxometalates. In the past, these metal oxide clusters have been used as model systems in molecular magnetism because of their ability to host magnetic ions in chemically tailored environments of high symmetry and rigidity¹⁷. Currently, these molecules are seen as potential building blocks in quantum computing architectures^{18–22}.

In the present study we chose the $[\text{Ho}(\text{W}_5\text{O}_{18})_2]^{9-}$ complex (abbreviated HoW₁₀), which has been subjected to extensive structural, magnetic and spectroscopic characterizations that raised the possibility of observing coherent spin dynamics^{23,24}. HoW₁₀ is formed by two molecular tungsten oxide moieties encapsulating a Ho³⁺ ion (Fig. 1). The geometry around Ho³⁺ exhibits a slightly distorted square-antiprismatic environment, which can be approximated by a

D_{4d} ‘pseudo-axial’ symmetry. This results in a splitting of the total angular momentum, $J=8$, ground state spin-orbit manifold according to its m_J quantum numbers. Quantitatively this splitting can be described by the spin Hamiltonian in equation (1), where the double summation parameterizes the crystal-field (CF) interaction which, for D_{4d} symmetry, contains the axial terms $B_2^0\hat{O}_2^0$, $B_4^0\hat{O}_4^0$ and $B_6^0\hat{O}_6^0$ (see Methods for definition and discussion of terms in equation (1)²⁴)

$$\hat{H} = \sum_{k=2,4,6} \sum_{q=0}^k B_k^q \hat{O}_k^q + \hat{J} \cdot A \cdot \hat{I} + \mu_B \mathbf{B}_0 \cdot g_L \cdot \hat{J} - \mu_N g_N \mathbf{B}_0 \cdot \hat{I} \quad (1)$$

This results in an isolated $m_J = \pm 4$ ground doublet, separated from the first excited states ($m_J = \pm 5$) by $\sim 20 \text{ cm}^{-1}$. This picture provides a reasonable description of the magnetic properties of this molecule²³. However, minor deviations from D_{4d} symmetry that are present in the crystal make operative the tetragonal $B_4^4\hat{O}_4^4$ CF interaction. Interestingly, the match between the (\pm integer) values of the ground state spin projections, $m_J = \pm 4$, and the tetragonal (that is, $q=4$) order of the main symmetry axis of the molecule results in the $B_4^4\hat{O}_4^4$ (here $\hat{O}_4^4 = \frac{1}{2}(\hat{J}_+^4 + \hat{J}_-^4)$) interaction generating an unusually large quantum tunnelling gap, $\Delta \approx 9.18 \text{ GHz}$ ($\sim 0.3 \text{ cm}^{-1}$)²⁴. This gap is a crucial factor for the coherence of electron spin dynamics in molecular spin qubits, and is the main subject of the present study.

The standard approach to probing coherent spin dynamics involves the use of electron spin echoes in pulsed electron paramagnetic resonance (EPR). The HoW₁₀ system is attractive in this regard because its predicted tunnelling gap ($\sim 9.18 \text{ GHz}$, Fig. 1) is close to the X-band frequency associated with the most sophisticated EPR spectrometers. While the magnitude of the gap is set by B_4^4 , interesting details of the EPR spectra are also determined by the hyperfine interaction between the Ho electron and nuclear spins (the second term in equation (1)). Holmium occurs naturally in only one stable isotope (¹⁶⁵Ho) with a nuclear spin of $I = 7/2$. A strong hyperfine coupling ($A_{\parallel} = 830 \pm 10 \text{ MHz}$) results in the observation of eight ($2I + 1$) well-resolved transitions via continuous-wave (CW) high-frequency EPR measurements²⁴. The energy level scheme that arises from the combination of CF and hyperfine coupling, together with the Zeeman interaction (third and fourth terms in equation (1)), gives rise to a series of avoided level crossings between $m_J = \pm 4$ states (with the same m_I), resulting in multiple gaps in the energy diagram near zero field (Fig. 1a).

Single crystals of $\text{Na}_9[\text{Ho}_x\text{Y}_{(1-x)}(\text{W}_5\text{O}_{18})_2] \cdot n\text{H}_2\text{O}$ (where Y (yttrium) is non-magnetic) were prepared with Ho concentrations ranging from $x = 0.25$ to $x = 0.001$, that is, up to three orders of magnitude away from the usual high-dilution limit¹⁰, allowing a study of the effects of dilution on electron dipolar spin-spin decoherence. Figure 2a displays electron-spin-echo- (ESE-) detected EPR spectra recorded at 5 K for a dilute ($x = 0.001$) sample at frequencies from 9.1 GHz to 9.8 GHz, with $\theta = 29^\circ$ (θ is the angle between the applied field, \mathbf{B}_0 , and the z axis

¹National High Magnetic Field Laboratory and Department of Physics, Florida State University, Tallahassee, Florida 32310, USA. ²Instituto de Ciencia Molecular, Universidad de Valencia, C/Catedrático José Beltrán 2, 46980 Paterna, Spain.

*These authors contributed equally to this work.

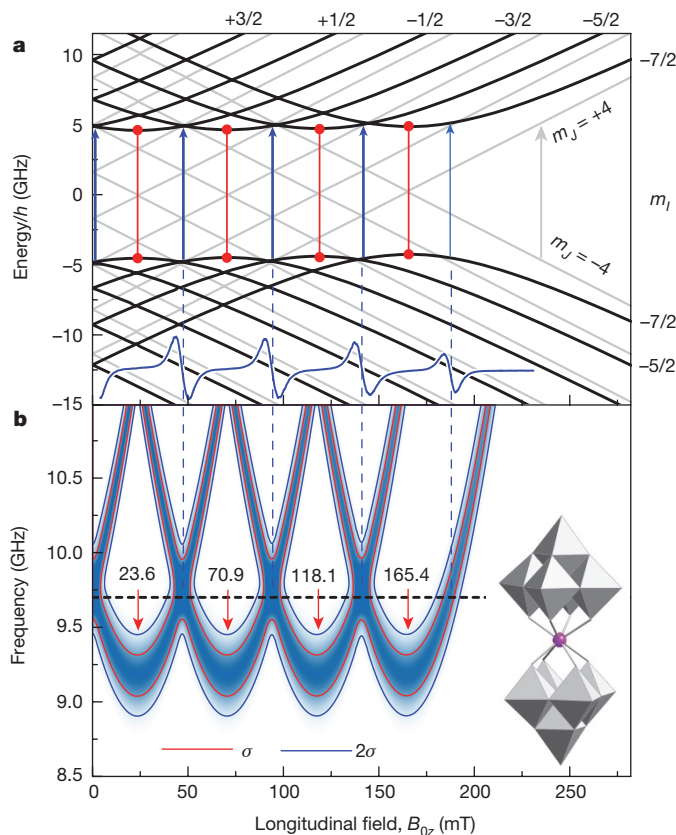


Figure 1 | HoW₁₀ tunnelling gap. **a**, Main figure, Zeeman diagrams for the $m_J = \pm 4$, $I = 7/2$ ground state, with $B_{0\parallel z}$: the thin grey lines assume exact D_{4d} symmetry, while the thick black curves assume an ‘axial + $B_4^4 \hat{O}_4^4$ ’ parameterization²⁴. Numbers on the top and right axes indicate m_l values. Inset (blue trace at bottom), the corresponding 9.64 GHz CW EPR spectrum (reproduced from figure 8 of ref. 24 with permission from the Royal Society of Chemistry) is observed well below the D_{4d} prediction (grey arrow denotes expected highest field resonance), providing evidence for the tunnelling gap. Indeed, the ‘axial + $B_4^4 \hat{O}_4^4$ ’ parameterization gives excellent agreement with the data, both in terms of resonance positions (blue arrows) and intensity (arrow thickness). The red vertical lines, meanwhile, indicate the locations of CTs. **b**, Main figure, 3D EPR intensity map including inhomogeneous broadening due to a Gaussian distribution in B_4^4 ($\sigma_{B44} = 2.1 \times 10^{-5} \text{ cm}^{-1}$); darker shading represents stronger intensity, with contours at the $\pm\sigma_{\Delta}$ (red) and $\pm 2\sigma_{\Delta}$ (blue) levels ($\sigma_{\Delta} = 123 \text{ MHz}$, the s.d. in Δ). Red arrows denote CTs and dashed lines denote locations of 9.64 GHz resonances. Inset, the HoW₁₀ molecule.

of the crystal); ESE signals were generated using a two-pulse Hahn-echo sequence (see Methods)²⁵. Four broad peaks of equal intensity are observed at the two lowest frequencies (9.11 GHz and 9.16 GHz), which were selected to be close to the gap minima in Fig. 1b. With increasing frequency, these peaks split and move symmetrically apart, as expected on the basis of predictions in Fig. 1b. For the most part, the data lie on the simulated curves, with the obvious exception of the two lowest frequencies and some lower-field (<60 mT) data points. The simulations are based on previously determined Hamiltonian parameters²⁴, and the spectra are plotted against the re-scaled longitudinal applied field, $B_{0z} (= B_0 \cos \theta)$, to facilitate comparisons between different samples (see Methods).

Two-pulse ESE measurements were separately used to determine 5 K transverse relaxation times, T_2 , at selected points within the spectrum for the $x = 0.001$ concentration. The longest values of T_2 are found in the vicinity of the gap minima (at $B_{0z} = B_{\min}$) for the smallest crystals (see Figs 2b, 3 and Methods), with values ranging from 5.2 μs to 8.4 μs , whereas the values are substantially shorter away from the minima. In fact, the T_2 values exhibit sharp divergences right at B_{\min} (Fig. 3). The key to understanding this behaviour is the quadratic field dependence

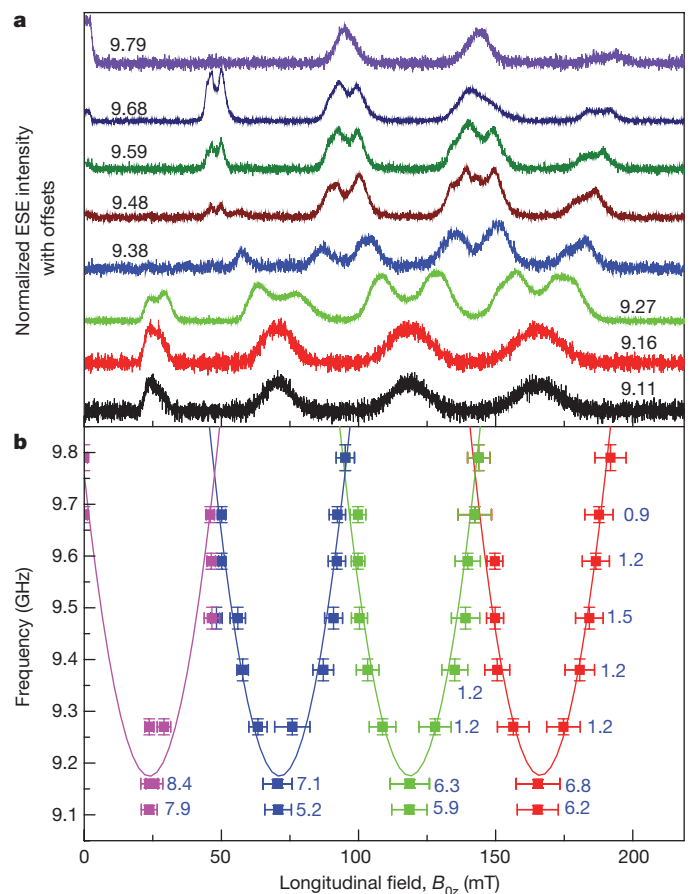


Figure 2 | ESE-detected spectra for a dilute sample. **a**, Variable frequency measurements at 5.0 K for an $x = 0.001$ crystal, with $\theta = 29^\circ$; the frequencies are indicated in GHz above each trace. **b**, Frequency versus field plot of the resonances in **a**. The data are in good agreement with simulations (solid curves) based on the ‘axial + $B_4^4 \hat{O}_4^4$ ’ parameterization²⁴. Selected T_2 values (in μs) determined from the measurements in Fig. 3 are indicated in blue close to some of the data points. Vertical error bars in **b** denote pulse excitation bandwidths ($\pm 1/2\tau_{\pi/2}$, where $\tau_{\pi/2}$ is the duration of the $\pi/2$ pulse), while horizontal error bars represent standard deviations (\pm s.d.) deduced from Gaussian fits to the resonances in **a**.

of the EPR transition frequencies (f) close to the gap minima (see Methods)

$$f = \Delta + \frac{\gamma_z^2}{2\Delta} (B_{0z} - B_{\min})^2 \quad (2)$$

such that the derivative $df/dB_{0z} \propto (B_{0z} - B_{\min}) \rightarrow 0$ as $B_{0z} \rightarrow B_{\min}$; here, γ_z is the z component of the gyromagnetic tensor. Although not explicitly included in equation (1), nearly all sources of dipolar decoherence (due, for example, to dynamics associated with the nuclear bath and collective electron spin excitations, or magnons) can be approximated as a time-dependent magnetic noise, $\delta B_0(t)$, acting on the central spin qubit (the spin being measured) via the Zeeman interaction. In other words, processes that flip nearby spins cause variations in the local field, δB_0 , at the position of the central spin, thereby altering its frequency/phase. Many of these processes involve indirect pairwise spin flip-flops (spin diffusion) that are extremely hard to mitigate, and persist to very low temperatures. The extreme axial anisotropy of HoW₁₀ results in an insensitivity to the perpendicular applied field component, $B_{0\perp}$ (see Methods). Meanwhile, sensitivity to $\delta B_{0z}(t)$ vanishes (to first order) as $B_{0z} \rightarrow B_{\min}$ and $df/dB_{0z} \rightarrow 0$, resulting in a vanishing contribution to the dipolar decoherence. This is the concept behind ‘atomic clock transitions’. Named after the principle which gives atomic clocks their exceptional phase

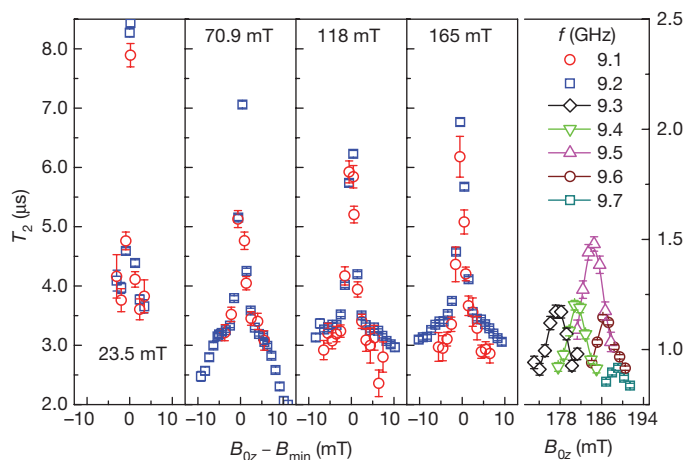


Figure 3 | T_2 divergence at the CTs. Field-swept T_2 measurements recorded at 5.0 K for a small $x = 0.001$ crystal at $\theta = 22^\circ$ and various frequencies indicated in the key in the rightmost panel. The first four panels illustrate the divergences in T_2 at the CTs, referenced to the left-hand ordinate; the data are plotted in an expanded view as a function of $(B_{0z} - B_{\min})$, with best-fit B_{\min} values given in each panel. The rightmost panel, meanwhile, displays T_2 values well away from the CTs (see Fig. 1b), referenced to the right-hand ordinate. Error bars denote the standard error in T_2 .

stability, these transitions are protected against environmental noise, resulting in dramatically enhanced quantum coherence^{26,27}. Indeed, one expects the dephasing time, T_2 , to scale as $(B_{0z} - B_{\min})^{-n}$ ($n > 0$, see Extended Data Fig. 1)^{28,29}, thus explaining the observed divergences at the clock transitions (CTs). For comparison, T_2 measurements are displayed in the rightmost panel of Fig. 3 for several ‘normal’ EPR transitions, that is, $m_j = -4$ to $+4$ transitions away from the gap minima, where the frequency dependence approaches the linear regime and $d f/dB_{0z} \rightarrow \gamma_z = 139.9 \text{ GHz T}^{-1}$ (Fig. 1). Although T_2 is moderately peaked at the centres of these resonances, the sharp divergences seen at the CTs are clearly absent (see Methods for further discussion).

ESE-detected measurements for an $x = 0.01$ sample reveal divergences in T_2 at the CTs that are essentially identical to those seen in Fig. 3, with maximum values ranging from $4 \mu\text{s}$ to $8 \mu\text{s}$ (see Extended Data Figs 1 and 2). However, T_2 values associated with ‘normal’ EPR transitions well away from the CTs are much shorter ($\sim 100 \text{ ns}$, not shown). Because the collection of ESE spectra requires the detection of an echo, the observation of these ‘normal’ EPR transitions is challenging for $x \geq 0.01$. These findings are consistent with the idea that dipolar ‘noise’ increases with increasing Ho concentration, resulting in shorter T_2 s for the ‘normal’ EPR transitions, yet there is an apparent insensitivity of T_2 to the Ho concentration right at the CTs.

Figure 4 displays 5 K ESE-detected spectra for a concentrated $x = 0.1$ sample that are in stark contrast to those in Fig. 2: narrow resonances are observed at the CTs that do not shift at all with frequency, that is, the data do not follow the simulations even though CW measurements indicate no measurable variation in the spin Hamiltonian parameters with Ho concentration²⁴. The total suppression of ‘normal’ EPR transitions is attributed to a further reduction of T_2 on increasing the Ho concentration, to the extent that an echo can no longer be detected. Nevertheless, the T_2 values at the CTs remain long ($\sim 0.7 \mu\text{s}$), resulting in the narrow ESE-detected resonances. Indeed, because the echo intensity is T_2 -weighted, the resonance lineshape is a direct manifestation of the field dependence of T_2 at B_{\min} . Analysis of CW EPR spectra suggests that the main contribution to the linewidth is a Gaussian distribution in the B_4^4 parameter ($\sigma_{B_{44}} = 0.63 \text{ MHz}$). This causes significant vertical broadening of the tunnelling gap, Δ , and EPR transition frequencies, as illustrated in Fig. 1b, which includes contours at the $\pm\sigma_\Delta$ and $\pm 2\sigma_\Delta$ levels ($\sigma_\Delta = 123 \text{ MHz}$ is the standard deviation in Δ ; see Methods). These simulations indicate measurable intensity at

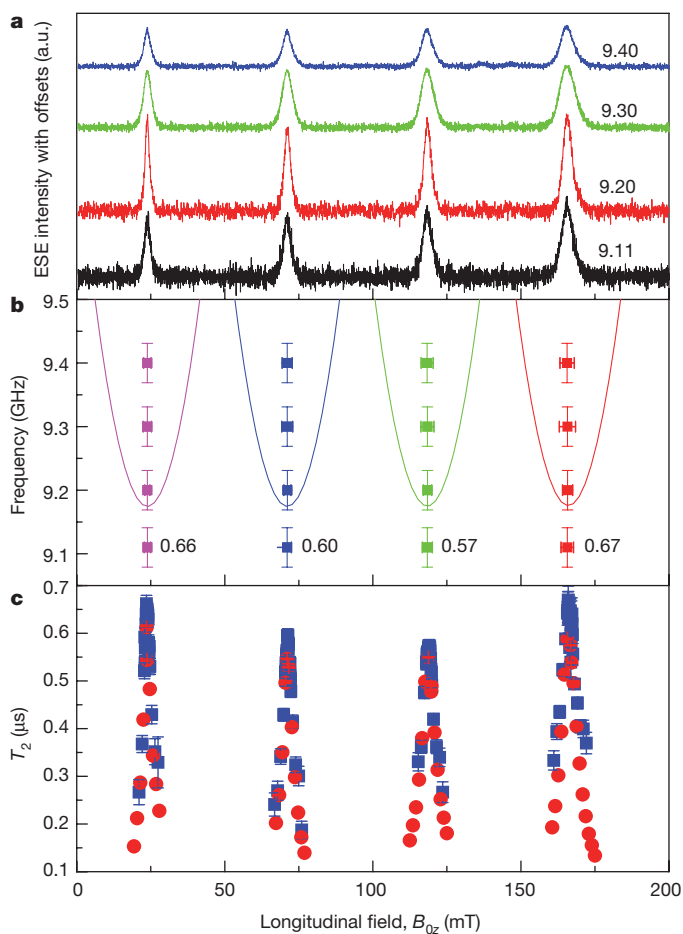


Figure 4 | ESE-detected spectra for a concentrated sample. **a**, Variable frequency measurements at 5.0 K for an $x = 0.10$ crystal, with $\theta = 20^\circ$; the frequencies are indicated in GHz above each trace. The ESE resonances are attributed to CTs. a.u., arbitrary units. **b**, Frequency versus field plot of the CTs in **a**. Optimum T_2 values (in μs) are indicated next to the 9.11 GHz data. Meanwhile, the curves correspond to predictions based on the CW EPR parameterization²⁴. **c**, Field-swept T_2 measurements recorded at 5.0 K for a separate $x = 0.10$ crystal at $\theta = 25^\circ$ and frequencies of 9.12 GHz (blue squares) and 9.20 GHz (red circles). Vertical error bars in **b** denote pulse excitation bandwidths ($\pm 1/2\tau_{\pi/2}$, where $\tau_{\pi/2}$ is the duration of the $\pi/2$ pulse), while horizontal error bars represent standard deviations ($\pm \text{s.d.}$) deduced from Gaussian fits to the resonances in **a**. Error bars in **c** denote the standard error in T_2 .

the CTs up to at least 9.4 GHz. However, the B_4^4 distribution does not shift the CTs appreciably to lower or higher fields, that is, all molecules in the distribution have their CTs at essentially the same B_{\min} values. This explains the observation of narrow CT peaks spanning a wide frequency range in the $x = 0.1$ sample (Fig. 4); similar behaviour is also discernible at other concentrations (see Extended Data Fig. 3).

After magnetic ‘noise’, other sources of decoherence remain. First, the CTs do not protect against direct flip-flop processes that involve the central spin qubit^{28,29}. These energy-conserving events involve coupling to other spins via the off-diagonal component of the dipolar interaction ($\hat{J}_2^+ \hat{J}_2 + \hat{J}_1^+ \hat{J}_2^+$). The inhomogeneous broadening will provide some protection against this source of dephasing, because it requires the central spin to be resonant with other spins. Nevertheless, direct flip-flops probably explain the shorter T_2 s at the CTs in the $x = 0.1$ sample. However, unlike the aforementioned indirect spin diffusion processes, direct flip-flops can be controlled at the stage of device design through the tuning/detuning of individual CT frequencies. Second, coupling of the Ho spin to lattice dynamics (phonons) via the CF is also likely to provide significant decoherence pathways, particularly as the temperature is raised^{9,16}. Indeed, a significant

temperature dependence of T_2 is found at the CTs (a decrease by a factor of more than 2 upon heating the sample to 7 K), suggesting that T_2 may become limited by the spin–lattice relaxation time, T_1 ($\sim 20 \mu\text{s}$ at 5 K). This is something that will be the subject of future investigations.

The critical result from this study is the demonstration that CTs can be employed as a means of enhancing the coherence of molecular spin qubits in concentrated samples. Therefore, instead of attempting to suppress magnetic noise, which can be impractical at the stage of device design, we have shown here that one can fortify the molecular spin qubit itself against this noise through the use of CTs. In terms of design criteria, the molecule of choice should possess a large tunnelling gap within the ground magnetic doublet that matches the working frequency of the EPR cavity. The key to this strategy is the chemical design of molecular structures with appropriate CF states. In rare-earth complexes with integer spin, this goal translates into matching the m_j components of the ground doublet with the rotational order (q) of the main symmetry axis of the molecule (see Methods). Although this is not trivial to achieve, the case of HoW_{10} is not an isolated example. For example, within rigid polyoxometalate chemistry, the terbium derivative of the $[\text{LnP}_5\text{W}_{30}\text{O}_{110}]^{12-}$ series (where Ln indicates lanthanide) with pentagonal structure (approximate C_{5v} symmetry) has been characterized as having an $m_j = \pm 5$ ground state with an even larger tunnelling gap of ~ 21 GHz that may be suitable for pulsed Q-band EPR³⁰. Tunability across this range (10–100 GHz) is desirable and practical for quantum information applications, given that it matches the clock rate of state-of-the-art microprocessors. Moreover, operation at these CTs requires application of only very moderate magnetic fields (< 0.2 T in the present example). Of course, this strategy can and should be combined with other ideas that are already being applied with success, such as using rigid lattices with a low abundance of nuclear spins¹⁶. Nevertheless, it is remarkable that working with CTs offers the unique advantage of allowing long coherence times with high concentrations of molecular spin qubits. In fact, for other molecular spin qubit candidates, T_2 values of the order of tens of microseconds were only observable in deuterated and highly diluted samples of Cr_7Ni molecular wheels¹⁰ and $\text{Cu}(\text{mnt})_2$ ($\text{mnt} = \text{maleonitriledithiolate}$) complexes¹⁶.

Online Content Methods, along with any additional Extended Data display items and Source Data, are available in the online version of the paper; references unique to these sections appear only in the online paper.

Received 2 September 2015; accepted 5 January 2016.

- Schlosshauer, M. A. *Decoherence and the Quantum-To-Classical Transition* (Springer, 2008).
- Stamp, P. C. E. Quantum information: stopping the rot. *Nature* **453**, 167–168 (2008).
- Devoret, M. H. & Schoelkopf, R. J. Superconducting circuits for quantum information: an outlook. *Science* **339**, 1169–1174 (2013).
- Duan, L. Quantum physics: a strong hybrid couple. *Nature* **508**, 195–196 (2014).
- Weitenberg, C. *et al.* Single-spin addressing in an atomic Mott insulator. *Nature* **471**, 319–324 (2011).
- Pla, J. J. *et al.* A single-atom electron spin qubit in silicon. *Nature* **489**, 541–545 (2012).
- Taminiau, T. H., Cramer, J., van der Sar, T., Dobrovitski, V. V. & Hanson, R. Universal control and error correction in multi-qubit spin registers in diamond. *Nature Nanotechnol.* **9**, 171–176 (2014).
- Ardavan, A. *et al.* Will spin-relaxation times in molecular magnets permit quantum information processing? *Phys. Rev. Lett.* **98**, 057201 (2007).
- Takahashi, S. *et al.* Decoherence in crystals of quantum molecular magnets. *Nature* **476**, 76–79 (2011).

- Kaminski, D. *et al.* Quantum spin coherence in halogen-modified Cr_7Ni molecular nanomagnets. *Phys. Rev. B* **90**, 184419 (2014).
- Wedge, C. J. *et al.* Chemical engineering of molecular qubits. *Phys. Rev. Lett.* **108**, 107204 (2012).
- Leuenberger, M. N. & Loss, D. Quantum computing in molecular magnets. *Nature* **410**, 789–793 (2001).
- Warner, M. *et al.* Potential for spin-based information processing in a thin-film molecular semiconductor. *Nature* **503**, 504–508 (2013).
- Graham, M. *et al.* Influence of electronic spin and spin-orbit coupling on decoherence in mononuclear transition metal complexes. *J. Am. Chem. Soc.* **136**, 7623–7626 (2014).
- Thiele, S. *et al.* Electrically driven nuclear spin resonance in single-molecule magnets. *Science* **344**, 1135–1138 (2014).
- Bader, K. *et al.* Room temperature quantum coherence in a potential molecular qubit. *Nature Commun.* **5**, 5304 (2014).
- Clemente-Juan, J. M. & Coronado, E. Magnetic clusters from polyoxometalate complexes. *Coord. Chem. Rev.* **193–195**, 361–394 (1999).
- Clemente-Juan, J. M., Coronado, E. & Gaita-Ariño, A. Magnetic polyoxometalates: from molecular magnetism to molecular spintronics and quantum computing. *Chem. Soc. Rev.* **41**, 7464–7478 (2012).
- Lehmann, L., Gaita-Ariño, A., Coronado, E. & Loss, D. Spin qubits with electrically gated polyoxometalate molecules. *Nature Nanotechnol.* **2**, 312–317 (2007).
- van Hoogdalem, K., Stepanenko, D. & Loss, D. In *Molecular Magnets: Physics and Applications* (eds Bartolomé, J. *et al.*) 275–296 (Springer, 2014).
- Aldamen, M. A., Clemente-Juan, J. M., Coronado, E., Martí-Gastaldo, C. & Gaita-Ariño, A. Mononuclear lanthanide single-molecule magnets based on polyoxometalates. *J. Am. Chem. Soc.* **130**, 8874–8875 (2008).
- Martínez-Pérez, M. J. *et al.* Gd-based single-ion magnets with tunable magnetic anisotropy: molecular design of spin qubits. *Phys. Rev. Lett.* **108**, 247213 (2012).
- Aldamen, M. A. *et al.* Mononuclear lanthanide single molecule magnets based on the polyoxometalates $[\text{Ln}(\text{W}_5\text{O}_{18})_2]^{9-}$ and $[\text{Ln}(\beta\text{-SiW}_{11}\text{O}_{39})_2]^{13-}$ ($\text{Ln}^{\text{III}} = \text{Tb}, \text{Dy}, \text{Ho}, \text{Er}, \text{Tm}, \text{and Yb}$). *Inorg. Chem.* **48**, 3467–3479 (2009).
- Ghosh, S. *et al.* Multi-frequency EPR studies of a mononuclear holmium single-molecule magnet based on the polyoxometalate $[\text{Ho}^{\text{III}}(\text{W}_5\text{O}_{18})_2]^{9-}$. *Dalton Trans.* **41**, 13697–13704 (2012).
- Schweiger, A. & Jeschke, G. *Principles of Pulse Electron Paramagnetic Resonance* (Oxford Univ. Press, 2001).
- Bollinger, J. J. *et al.* Laser-cooled-atomic frequency standard. *Phys. Rev. Lett.* **54**, 1000–1003 (1985).
- Vion, D. *et al.* Manipulating the quantum state of an electrical circuit. *Science* **296**, 886–889 (2002).
- Wolfowicz, G. *et al.* Atomic clock transitions in silicon-based spin qubits. *Nature Nanotechnol.* **8**, 561–564 (2013).
- Balian, S. J., Wolfowicz, G., Morton, J. J. L. & Monteiro, T. S. Quantum bath-driven decoherence of mixed spin systems. *Phys. Rev. B* **89**, 045403 (2014).
- Cardona-Serra, S. *et al.* Lanthanoid single-ion magnets based on polyoxometalates with a 5-fold symmetry: the series $[\text{LnP}_5\text{W}_{30}\text{O}_{110}]^{12-}$ ($\text{Ln}^{3+} = \text{Tb}, \text{Dy}, \text{Ho}, \text{Er}, \text{Tm}, \text{and Yb}$). *J. Am. Chem. Soc.* **134**, 14982–14990 (2012).

Acknowledgements We thank L. Song and J. van Tol for technical assistance with the X-band EPR spectrometer. This work was supported by the NSF (grant DMR-1309463) and the US AFOSR (AOARD contract 134031 FA2386-13-1-4029). Work performed at the NIMFL was supported by the NSF (DMR-1157490) and by the State of Florida. Work performed at the Instituto de Ciencia Molecular was supported by the European Research Council (grants SPINMOL and DECRESIM), by the Spanish MINECO (projects MAT-2014-56143-R, CTQ2014-52758-P and Excellence Unit Maria de Maeztu MDM-2015-0538) and by the Generalitat Valenciana (Prometeo and ISIC-Nano Programs of Excellence). A.G.-A. thanks the Spanish MINECO for a Ramón y Cajal Fellowship.

Author Contributions S.H., E.C. and A.G.-A. conceived the research and wrote the paper. Y.D. prepared the samples. S.H., M.S. and D.K. designed the experiments, while M.S. and D.K. performed the measurements. S.H., M.S. and D.K. analysed the results.

Author Information Reprints and permissions information is available at www.nature.com/reprints. The authors declare no competing financial interests. Readers are welcome to comment on the online version of the paper. Correspondence and requests for materials should be addressed to S.H. (shill@magnet.fsu.edu) or E.C. (eugenio.coronado@uv.es).

METHODS

Experimental details. Pulsed EPR measurements were performed on a commercial Bruker E680 X-band spectrometer equipped with a cylindrical TE₀₁₁ dielectric resonator (model ER 4118 X-MD5) with a centre frequency $f_0 = 9.75$ GHz. Single-crystals of Na₉[Ho_xY_(1-x)(W₅O₁₈)₂·nH₂O ($x = 0.001$ to 0.25) were prepared according to the method described in ref. 23. Samples were re-crystallized before study, then transferred to the spectrometer directly from the mother liquor and cooled rapidly in order to prevent loss of crystallinity due to evaporation of lattice solvent. The sample temperature was controlled using an Oxford Instruments CF935 helium flow cryostat and ITC503 temperature controller. A strong temperature dependence of T_2 at the CTs required operation of the cryostat at a temperature of 5.0 K in order to ensure good thermal stability and sample-to-sample reproducibility.

For each series of measurements, a single crystal was mounted on a 4 mm diameter quartz rod and positioned at the centre of the cylindrical resonator for perpendicular mode excitation. The tendency for samples to rapidly lose solvent, and the low symmetry $P\bar{1}$ space group of the HoW₁₀ compound, made it impossible to index and align crystals before mounting. However, the Bruker E680 and ER 4118X-MD5 dielectric resonator combination allows for *in situ* sample rotation about a single axis. Each crystal was therefore aligned as best as possible on the basis of angle-dependent CW EPR measurements performed at 9.75 GHz and 5.0 K. The remaining misalignment, θ , between \mathbf{B}_0 and z was determined by scaling the applied field to match the simulations in Fig. 1 (see below). A $\theta < 30^\circ$ criterion was then applied; crystals not meeting this condition were discarded and a new sample selected for study.

When overcoupled for ESE measurements, the bandwidth of the resonator is given by $\Delta f = f_0/Q \approx 250$ MHz, where the loaded quality factor $Q \approx 40$. This is sufficient to allow variable-frequency measurements with reasonable microwave B_1 fields down to a lower limit of ~ 9.1 GHz. The B_1 fields were independently measured under the same conditions via the Rabi oscillation frequency (Ω_R) of a spin-1/2 EPR standard (the organic radical bisdiphenylene-2-phenylallyl dissolved in polystyrene); B_1 values varied from ~ 4 G at 9.1 GHz, to 9 G at 9.75 GHz ($\Omega_R = 11\text{--}25$ MHz for $s = 1/2$). A two-pulse sequence ($T/2\text{--}\tau\text{--}T\text{--}\tau\text{--}\text{echo}$), where T characterizes the pulse durations and τ the delay time between pulses) was employed for all ESE measurements reported in this work. The values of T , τ and the source power were optimized at each frequency, with the assumption that the optimum conditions correspond approximately to the Hahn-echo sequence, $\pi/2\text{--}\tau\text{--}\pi\text{--}\tau\text{--}\text{echo}$, where π refers to the tipping angle. For T_2 measurements, τ was varied and the resultant echo amplitude then fitted to a single exponential decay.

Pulse sequences. Because the ESE measurements were performed well below the centre frequency of the cavity, and owing to the lack of a priori knowledge of the matrix elements associated with the observed transitions, pulse sequences were adjusted at each frequency by one of two methods: (1) the $\pi/2$ pulse length ($T/2$) and source attenuation were adjusted to maximize the echo intensity relative to the spectrometer noise for the ESE-detected spectra in Figs 2a and 4a, thereby explaining the variability of the vertical error bars denoting excitation bandwidth (defined as $2/T$, or $1/\tau_{\pi/2}$, where $\tau_{\pi/2}$ is the duration of the $\pi/2$ pulse in the Hahn-echo sequence); and (2) Rabi oscillation measurements were used to determine the optimum $\pi/2$ pulse length for the detailed T_2 measurements displayed in Figs 3 and 4c, and Extended Data Figs 1 and 2 (the Rabi pulse sequence was optimized via method (1)). On this basis, a Rabi frequency, $\Omega_R = 98$ Mrad s^{-1} (15.6 MHz), was determined for 0 dB attenuation at the CTs, resulting in a minimum $\pi/2$ pulse length of 16 ns for the employed spectrometer. This corresponds to an optimum dephasing factor $Q_\varphi = 820$, defined here as $Q_\varphi = \Omega_R T_2$, a figure of merit for qubit operation. We note, however, that this does not preclude shorter pulses using a more powerful microwave source, suggesting the possibility of Q_φ values up to 1.5×10^6 using the modified definition in ref. 9. Interestingly, this value is identical to the one reported in ref. 9 for an Fe₈ nanomagnet, in spite of the vastly different frequencies employed in the two measurements, primarily because of the much longer coherence in the HoW₁₀ system. Based on knowledge of the spectrometer used for the Fe₈ study, we estimate a $Q_\varphi = \Omega_R T_2$ of just 50 for Fe₈; of course, the same arguments concerning limited source power apply in that case. The HoW₁₀ Q_φ value compares favourably with other candidate molecular spin qubits using both definitions—for example, the optimum $Q_\varphi (= \Omega_R T_2)$ varies from $\sim 2,000$ for the Cr₇Ni wheel (ref. 10), up to $\sim 10,000$ obtained recently for a Cu^{II} coordination complex¹⁶. However, one should bear in mind that extreme dilution/deuteration was employed in these cases.

The spin Hamiltonian. The energy spectrum associated with the Hund's rule spin-orbit coupled ground state of the Ho³⁺ ion, with $L = 6$, $S = 2$ and $J = |\mathbf{L} + \mathbf{S}| = 8$, can be described by the effective Hamiltonian (equation (1) in the main text, reproduced here for convenience)

$$\hat{H} = \sum_{k=2,4,6} \sum_{q=0}^k B_k^q \hat{O}_k^q + \hat{J} \cdot \mathbf{A} \cdot \hat{I} + \mu_B \mathbf{B}_0 \cdot \mathbf{g}_L \cdot \hat{J} - \mu_N g_N \mathbf{B}_0 \cdot \hat{I}$$

The double summation describes the CF interaction in terms of extended Stevens operators \hat{O}_k^q ($k = 2, 4, 6$, and $|q| \leq k$), with associated coefficients B_k^q (refs 31, 32), and with \hat{O}_k^q expressed in terms of the total electronic angular momentum operators \hat{J} and \hat{J}_i ($i = x, y, z$). Using this convention, the axial ($q = 0$) coefficients determined from magnetic and continuous-wave (CW) EPR measurements are^{23,24}: $B_2^0 = 0.601 \text{ cm}^{-1}$, $B_4^0 = 6.96 \times 10^{-3} \text{ cm}^{-1}$, and $B_6^0 = -5.10 \times 10^{-5} \text{ cm}^{-1}$. This parameterization results in the $m_J = \pm 4$ CF states lying lowest in energy (Fig. 1), separated from the $m_J = \pm 5$ excited states by $\sim 20 \text{ cm}^{-1}$ (ref. 23). The second term in equation (1) describes the hyperfine coupling between the Ho³⁺ electron and $I = 7/2$ nuclear spin, resulting in the observation of eight $(2I + 1)$ well-resolved electro-nuclear transitions via high-field CW EPR measurements; here, \hat{I} denotes the total nuclear angular momentum operator, and \mathbf{A} the hyperfine coupling tensor, for which the parallel component, $A_{\parallel} = 830 \pm 10$ MHz, has been determined from the high-field CW EPR spectrum²⁴. The final two terms in equation (1) respectively parameterize the electron and nuclear Zeeman interactions with the local magnetic induction, \mathbf{B}_0 , in terms of a Landé g -tensor (g_L) and isotropic nuclear g -factor (g_N); μ_B and μ_N represent the Bohr (electron) and nuclear magneton, respectively. The parallel component of the Landé g -tensor, $g_z = 1.25(1)$, has been determined from CW EPR studies²⁴.

In addition to the axial ($q = 0$) CF parameters, CW EPR measurements at X-band frequencies can only be accounted for by including a sizeable tetragonal $B_4^4 \hat{O}_4^4$ ($\hat{O}_4^4 = \frac{1}{2}(\hat{J}_+^4 + \hat{J}_-^4)$) interaction, with $B_4^4 = 3.14 \times 10^{-3} \text{ cm}^{-1}$ (see Fig. 1a and ref. 24 for detailed explanation). It is this term (which is allowed because of a small distortion of the HoW₁₀ molecule away from exact D_{4d} symmetry) that generates avoided level crossings between $m_J = \pm 4$ states, as seen in Fig. 1a. In principle, the sixth order tetragonal $B_6^4 \hat{O}_6^4$ interaction is also symmetry allowed. However, \hat{O}_6^4 contains the commutator $[\hat{J}_z^2, (\hat{J}_+^4 + \hat{J}_-^4)]$ and is, thus, indistinguishable from \hat{O}_4^4 within the truncated $m_J = \pm 4$ ground doublet. Therefore, we employ only the $B_4^4 \hat{O}_4^4$ term to capture the effects of the distortion away from exact D_{4d} symmetry. The key point is that \hat{O}_4^4 connects the $m_J = \pm 4$ states in second-order, resulting in unusually large (~ 9 GHz) quantum tunnelling gaps. For $\mathbf{B}_0 \parallel z$, the frequencies of the resultant weakly allowed EPR transitions between these states then follow a field-dependence of the form (see Fig. 1b)

$$f = \sqrt{\Delta^2 + \gamma_z^2 (B_{0z} - B_{\min})^2} \approx \Delta + \frac{\gamma_z^2}{2\Delta} (B_{0z} - B_{\min})^2 \quad (3)$$

where the approximate quadratic expression applies for fields close to the gap minima, B_{\min} . Indeed, because \hat{O}_4^4 represents the only off-diagonal CF interaction in equation (1), an almost exact mapping of the first expression of equation (3) onto curves generated via exact diagonalization of equation (1) is possible, yielding the following parameters: $\Delta = 9.18$ GHz, $\gamma_z = 139.9 \text{ GHz T}^{-1}$ ($= 1.25 \times 8 \times \mu_B/\hbar$, that is, $g_z = 1.25$), and $B_{\min} = 23.6, 70.9, 118.1$ and 165.4 mT. This analysis assumes $\mathbf{B}_0 \parallel z$, while the experiments are typically performed with a small field misalignment ($\theta \neq 0$), as noted above. However, due to the extreme uniaxial symmetry of the HoW₁₀ molecule, the perpendicular component of the effective gyromagnetic tensor associated with the $m_J = \pm 4$ doublet, $\gamma_{\perp, \text{eff}} < 0.1 \text{ GHz T}^{-1}$ ($g_{\perp, \text{eff}} < 0.01$), resulting in a virtual insensitivity to the perpendicular component of the applied field ($B_{0\perp}$) over the range explored in this investigation; for comparison, note that $\gamma_{\text{proton}} \approx 0.04 \text{ GHz T}^{-1}$. For this reason, one can approximate the electronic Zeeman term in equation (1) using a scalar interaction of the form, $g_z \mu_B B_{0z} \hat{J}_z$ (where $B_{0z} = B_0 \cos\theta$). Equation (3) then applies quite generally at the gap minima, provided the applied field is rescaled to account for any misalignment. Hence all EPR spectra are plotted as a function of the longitudinal applied field component, B_{0z} . Importantly, the derivative $df/dB_{0z} \rightarrow 0$ (that is, $\gamma_{z, \text{eff}} \rightarrow 0$) as $B_{0z} \rightarrow B_{\min}$, resulting in an almost complete insensitivity of the EPR transition frequencies at the gap minima to magnetic noise associated with the environment, thus giving rise to the strong T_2 divergences at the CTs. However, the small yet finite $\gamma_{\perp, \text{eff}} (< 0.1 \text{ GHz T}^{-1})$ probably limits T_2 right at the CTs (within ± 0.5 G of B_{\min}) in these studies due to the unavoidable field misalignment. In fact, $\gamma_{\perp, \text{eff}} \rightarrow 0$ as $B_0 \sin\theta \rightarrow 0$, which may explain the longer T_2 values observed at the lowest field CTs in Fig. 3, and also suggests that longer T_2 s may be achievable in precisely aligned samples.

T_2 scaling. The data displayed in Fig. 3 were obtained for a small crystal of the most dilute sample ($x = 0.001$). It is the high quality of this crystal that results in the sharp T_2 peaks at all four CTs (all four B_{\min} locations). However, it gives weak ESE signals, making it challenging to perform a detailed analysis of the scaling of T_2 with B_{0z} . Careful T_2 measurements were therefore repeated for larger samples. Unfortunately, the larger crystals are susceptible to twinning that manifests as a broadening of spectral peaks and T_2 divergences, with the effect being most pronounced at the higher field CTs (see Fig. 2a). However, the first CT at $B_{\min} = 23.6$ mT often remains sharp (see below for explanation). Extended Data Fig. 1 displays T_2 measurements for the $x = 0.001$ and 0.01 concentrations, plotted

against $(B_{0z} - B_{\min})$ on both logarithmic (main panels) and linear (insets) scales. Similar to the data in Fig. 3, the T_2 peaks exhibit broad tails, with an apparent kink at $|B_{0z} - B_{\min}| \approx 2$ mT for the more dilute sample. However, when plotted on a log-log scale, the data follow a power law (to within the experimental uncertainty) spanning an order of magnitude in $(B_{0z} - B_{\min})$ for $x = 0.001$, and almost two orders of magnitude for $x = 0.01$, particularly on the high-field sides of the T_2 peaks. This apparent monotonic behaviour of the form $T_2 \propto (B_{0z} - B_{\min})^{-n}$ supports our assertion that the decoherence is dominated by dipolar field fluctuations that vanish as $d\mathbf{f}/dB_{0z} \rightarrow 0$. However, the exponent, n , is both sample-dependent ($n = 0.33$ and 0.46 , respectively, for $x = 0.001$ and 0.01), and different from previous predictions^{28,29}: $n = 1$ for indirect flip-flop processes (spin diffusion), and $n = 2$ for instantaneous diffusion²⁵. We believe that sample inhomogeneity is responsible for these differences in HoW₁₀, thus masking the intrinsic T_2 dependence on B_{0z} , causing obvious sample-to-sample variability. It is nevertheless interesting that a power-law scaling still holds, as opposed, for example, to Gaussian behaviour. This clearly merits further theoretical investigation.

Reduced ESE intensity and faster T_2 decay curves are part of the reason for the increased error bars and apparent broad tails seen in Fig. 3 and Extended Data Fig. 1. In addition, ESE-envelope-modulation (ESEEM)²⁵ is detectable in the decay curves recorded in these tails (not shown). However, only one to two heavily damped periods of oscillation can be seen, thus adding to the error in T_2 (not to mention a potential systematic error that is not taken into account in our analysis). It is these combined factors that likely explain the apparent kink in some of the data at $|B_{0z} - B_{\min}| \approx 2$ mT, as well as the weak variation in T_2 across the ‘normal’ transitions seen in the right-hand panel of Fig. 3. Interestingly, enough ESEEM periods can be detected to confirm that it is due to coupling to protons in the sample. Importantly, the ESEEM vanishes at the CTs, providing further strong evidence that the Ho³⁺ spin becomes decoupled from the surrounding dipolar spin bath as both $(B_{0z} - B_{\min})$ and $d\mathbf{f}/dB_{0z} \rightarrow 0$.

Spectral broadening. The EPR spectra of HoW₁₀ are inhomogeneously broadened²⁴, with the two main contributions originating from (i) crystal twinning and (ii) strain in the off-diagonal B_4^4 CF parameter.

(i) Crystals of HoW₁₀ form as long thin needles that tend to aggregate into aligned bundles. Separating single crystals from these bundles can be challenging, particularly given that removal of the samples from their mother liquor for periods of more than a few minutes leads to sample degradation. Even after separation, our measurements suggest varying degrees of mosaic spread, particularly for the larger crystals. Indeed, simulations of high-field CW EPR spectra (where the effects of the mosaicity are more pronounced than at X-band) employed a Gaussian orientational distribution with a full-width at half-maximum (FWHM) of 1°, albeit for a small crystal²⁴; the distribution is considerably broader for many of the samples employed for ESE measurements. Within the context of equation (2), this mode of disorder produces a spread in γ_z and the B_{\min} values, resulting in horizontal smearing of the energy levels in Fig. 1, as opposed to a vertical smearing produced by a distribution in B_4^4 (see below). The horizontal smearing becomes more pronounced at higher fields, akin to g -strain. Consequently, the EPR spectra often become broader with increasing field, as is clearly evident in Fig. 2, and less so in Fig. 4.

Although subtle, the effects of sample mosaicity are most pronounced at the CTs. The horizontal spread in the CTs results in a smearing of the divergence in T_2 . In general, the strongest/narrowest divergences were obtained for the smallest crystals, which have the smallest mosaic spread. It is for this reason that the data for the most dilute samples in Figs 2 and 3 were obtained for two different crystals: the large crystal employed in Fig. 2a did not produce particularly strong T_2 divergences, with maximum values reaching only ~ 2 μ s. Meanwhile, a smaller crystal was employed in Fig. 3: this sample gave very good echoes right at the CTs, in spite of its reduced spin count; however, its ESE spectra vanish into the noise upon moving appreciably away from the CTs. These trends can be attributed both to a T_2 weighting effect, which amplifies the otherwise weak ESE signals at the CTs for the more ordered (longer T_2) sample, and to the narrower mosaic distribution that further enhances echoes at the CTs. Multiple small samples were studied, and optimum T_2 values at the CTs in the 6–8 μ s range were found in nearly all cases for the $x = 0.001$ and 0.01 samples (see Fig. 3 and Extended Data Figs 1 and 2).

(ii) Other sources of inhomogeneous broadening include: strains in the spin Hamiltonian parameters (B_k^q , A and g_L), caused by microscopic disorder, and inhomogeneities in B_0 due to electron and nuclear dipolar fields. The latter may be ruled out as a major source of broadening at X-band (and 5 K) due to weak sample magnetization and the lack of any systematic dependence of the EPR linewidth on Ho concentration. Meanwhile, the only effect of the diagonal ($q = 0$) CF terms in equation (1) is to ensure an isolated $m_J = \pm 4$ doublet ground state with $\gamma_z = g_J \mu_B / h = 139.9$ GHz T^{-1} ($J = 8$ and $g_J = 1.25$). Other than that, the low energy

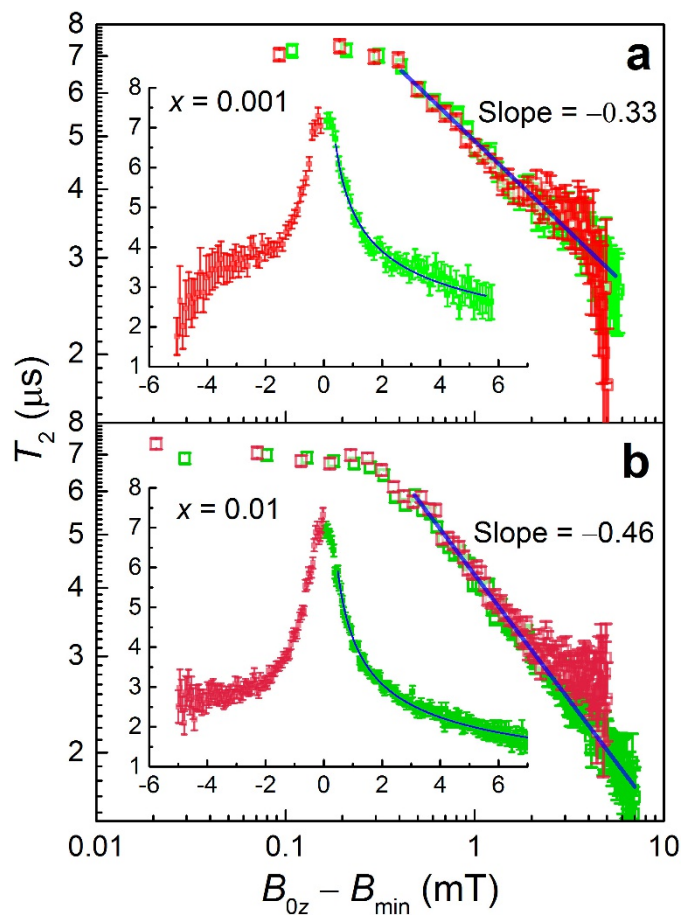
spectrum exhibits little or no dependence on B_2^0 , B_4^0 and B_6^0 (ref. 24), and should thus be insensitive to strains in these parameters. For related reasons, and because of the contracted nature of the $4f$ shell and strong spin-orbit coupling, the g_L and A tensors are relatively immune to local strains in the crystal structure (although the effective interactions will of course be sensitive to sample alignment due to the strong axial character of the CF). This leaves B_4^4 which, indeed, has a profound influence on the X-band EPR spectrum, as clearly seen in Fig. 1a and discussed in detail in ref. 24: B_4^4 directly sets the scale of the tunnelling gap, Δ , which is responsible for the CTs.

The finite B_4^4 parameter arises because of a small deviation of the coordination environment around the Ho ion from exact D_{4d} symmetry²⁴. The superposition of disorder onto this weakly distorted structure can then give rise to a relatively strong modulation of the local B_4^4 parameter and, hence, to a broad distribution for the ensemble. Working under this assumption, we re-simulated CW X-band spectra obtained for an $x = 0.1$ sample at a frequency of 9.64 GHz (figure 8 of ref. 24), assuming that the main source of broadening is a Gaussian distribution in B_4^4 . The best simulation is obtained with a FWHM of 5.0×10^{-5} cm⁻¹, that is, $\sim 1.6\%$ of B_4^4 (or a standard deviation, $\sigma_{B44} = 2.1 \times 10^{-5}$ cm⁻¹). This, in turn, produces a vertical distribution in the corresponding tunnelling gap, Δ . Because \hat{O}_4^4 connects the $m_J = \pm 4$ states at the second order of perturbation, the resultant standard deviation of the gap distribution is given approximately by $\sigma_{\Delta} \approx 2\Delta\sigma_{B44}/B_4^4 = 4.1 \times 10^{-3}$ cm⁻¹ = 123 MHz (FWHM of 290 MHz), where $\Delta = 0.306$ cm⁻¹ = 9.18 GHz is the mean gap value (the factor of ‘2’ emerges because of the quadratic dependence of Δ on B_4^4).

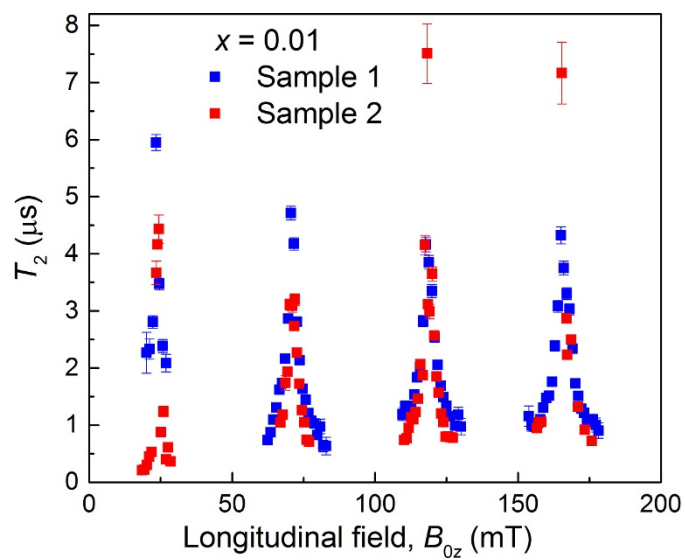
Figure 1b depicts the Gaussian broadening of the EPR transition frequencies as a 3D colour map, with contours shown at the $\pm\sigma_{\Delta}$ and $\pm 2\sigma_{\Delta}$ levels of the distribution. Because B_4^4 affects only Δ , this mode of disorder does not shift the magnetic fields (B_{\min}) at which the CTs occur for the different molecules in the distribution. However, it does distribute them vertically over a relatively wide frequency range (approximately ± 0.25 GHz at the $2\sigma_{\Delta}$ level). This can explain the observation of ESE intensity exactly at the CTs over a wide frequency range for the concentrated ($x = 0.1$) sample seen in Fig. 4. Because the cavity employed for these investigations has a centre frequency at 9.75 GHz, its sensitivity improves upon increasing the frequency from 9.1 to 9.4 GHz. Meanwhile, the number of Ho³⁺ spins in the distribution decreases with increasing frequency. These two factors approximately offset, explaining the relatively constant ESE intensity and signal-to-noise ratio across the studied frequency range. The ESE intensity does peak at 9.2 GHz, above which it decays, although not as rapidly as one may expect purely on the basis of the gap distribution. This is due to the increasing B_1 field of the spectrometer, which enables excitation of more spins and hence the generation of stronger echoes at higher frequencies.

This same behaviour is observable at the other concentrations. For example, CTs are very clearly observable in between the ‘normal’ EPR transitions over a wide frequency range at $B_{0z} = 165$ mT for the $x = 0.01$ sample, as seen in Extended Data Fig. 3. Further evidence can also be found at some of the higher frequencies, where inspection of Fig. 1a reveals crossings between nuclear sub-levels ($\Delta m_J = \pm 1$) at fields exactly half way between the B_{\min} values. If the applied field is not well aligned to the crystal z axis, these become avoided crossings (with < 10 MHz gaps), giving rise to new CTs at these higher frequencies. This is a subtlety of the perpendicular field component, $B_{0\perp}$, which will be the subject of a future publication. The avoided nuclear sub-level crossings do not influence any of the conclusions concerning the CTs at the B_4^4 gap minima (Δ). Nevertheless, the higher frequency CTs are observable, particularly at low fields where the effects of disorder due to sample mosaicity are less pronounced, and the ‘normal’ ESE transitions are quenched due to very short T_2 s (refs 2, 9). This is the explanation for the sharp double peaks seen for the $x = 0.001$ sample at ~ 50 mT between 9.4 and 9.7 GHz in Fig. 2a, as well as the sharp zero-field peaks and some of the fine structures seen between B_{\min} values at higher fields and frequencies. On the basis of the 50 mT CTs, one can see that the vertical broadening spans less than 400 MHz in this sample, that is, less than ± 200 MHz from the peak of the distribution. In other words, σ_{B44} clearly varies from sample to sample, being smaller for the $x = 0.001$ concentration. This is the reason why intensity due to the low-frequency CTs (at B_{\min}) is not discernible in between the broad ‘normal’ transitions in the most dilute sample in Fig. 2a.

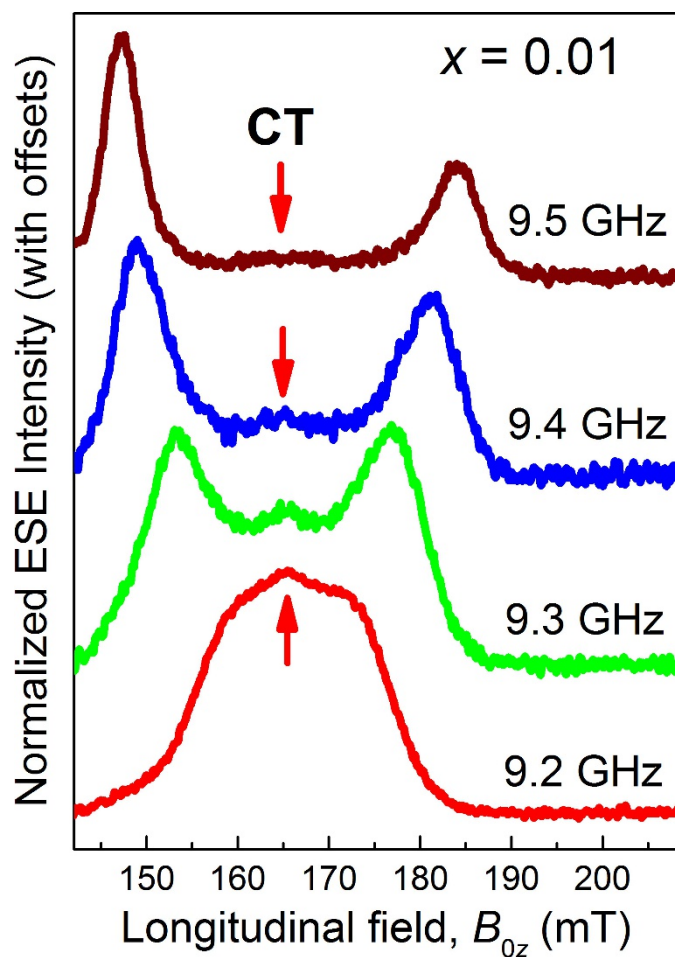
- Rudowicz, C. & Chung, C. Y. The generalization of the extended Stevens operators to higher ranks and spins, and a systematic review of the tables of the tensor operators and their matrix elements. *J. Phys. Condens. Matter* **16**, 5825–5847 (2004).
- Stoll, S. & Schweiger, A. EasySpin, a comprehensive software package for spectral simulation and analysis in EPR. *J. Magn. Reson.* **178**, 42–55 (2006).



Extended Data Figure 1 | T_2 scaling. **a, b,** Field-swept T_2 measurements for the $x = 0.001$ (**a**) and $x = 0.01$ (**b**) concentrations at 5 K; the data are plotted as a function of $(B_{0z} - B_{\min})$ on both log-log (main panels) and linear (insets) scales. The blue lines are power-law fits to the positive $(B_{0z} - B_{\min})$ data (green points), with the obtained exponents ('slope') given in the figures. Error bars, \pm standard error in T_2 .



Extended Data Figure 2 | T_2 divergence at the $x = 0.01$ concentration. Shown are field-swept T_2 measurements recorded at 5.0 K for two separate crystals at frequencies of 9.12 GHz (blue squares) and 9.20 GHz (red circles). Error bars, \pm standard error in T_2 .



Extended Data Figure 3 | ESE-detected spectra for the $x = 0.01$ concentration. Variable frequency measurements at 5.0 K, with $\theta = 30^\circ$; the frequencies are indicated above each trace. Similar to spectra for the $x = 0.001$ sample, the broad 9.2 GHz CT peak splits into two upon moving away from the tunnelling gap minimum (see also Fig. 2). However, weak ESE intensity can still be detected at $B_{0z} = 165$ mT at all four frequencies. This is due to vertical broadening of the CT, caused by a Gaussian distribution in B_4^4 .